Assimilation of snow water equivalent from AMSR2 and IMS satellite data utilizing the local ensemble transform Kalman filter

Joonlee lee[1], Myong-In Lee[1]*, Sunlae Tak[1], Eunkyo Seo[2,3], and Yong-Keun Lee[4]

[1] Department of Civil, Urban, Earth, and Environmental Engineering, Ulsan National Institute of Science and Technology, Ulsan, Korea

[2] Department of Environmental Atmospheric Sciences, Pukyong National University, Busan, South Korea.

[3] Center for Ocean-Land-Atmosphere Studies, George Mason University, Fairfax, VA, USA

[4] Earth System Science Interdisciplinary Center, University of Maryland, College Park, U.S.A.

20 SEP 2024

To be submitted to GMD

____

*Corresponding author: Prof. Myong-In Lee, Department of Urban and Environmental Engineering, Ulsan National Institute of Science and Technology, 50 UNIST-gil, Ulsan 44919, Republic of Korea (milee@unist.ac.kr)

Abstract

Snow Water Equivalent (SWE), as one of the land initial or boundary conditions, plays a crucial role in global or regional energy and water balance, thereby exerting a considerable impact on seasonal and sub-seasonal scale predictions owing to its enduring persistence over 1 to 2 months. Despite its importance, most SWE initialization remains challenging due to its reliance on simple approaches based on spatially limited observations. Therefore, this study developed the advanced SWE data assimilation framework with satellite remote-sensing data utilizing the local ensemble transform Kalman filter (LETKF) and the Joint U.K. Land Environment Simulator (JULES) land model. This approach constitutes an objective method that optimally combines two previously unattempted incomplete data sources: the satellite SWE retrieval from the Advanced Microwave Scanning Radiometer 2 (AMSR2) and dynamically-balanced SWE from the JULES land surface model. In this framework, an algorithm is additionally considered to determine the assimilation process based on the presence or absence of snow cover from the Interactive Multisensor Snow and Ice Mapping System (IMS) satellite, renowned for its superior reliability.

The baseline model simulation from JULES without satellite data assimilation shows better performance in high-latitude regions with heavy snow accumulation but relatively inferior in the transition regions with less snow and high spatial and temporal variation. Contrastingly, the AMSR2 satellite data exhibit better performance in the transition regions but poorer in the high latitudes, presumably due to the limitation of the satellite data in the penetrating depth. The data assimilation (DA) demonstrates the positive impacts by reducing uncertainty in the JULES model simulations in most areas, particularly in the mid-latitude transition regions. In the transition regions, the model background errors from the ensemble runs are significantly larger than the observation errors, emphasizing great uncertainty in the model simulations. The results of this study highlight the beneficial impact of data assimilation by effectively combining both

49 land surface model and satellite-derived data according to their relative uncertainty, thereby

50 controlling not only transitional regions but also the regions with heavy snow accumulation

51 that are difficult to detect by satellite.

52

1. Introduction

Snow plays a crucial role in regulating the water, energy, and carbon exchange between the land surface and atmosphere (e.g., Dutra et al., 2011; Thomas et al., 2016). A snowpack tends to increase surface albedo and soil moisture as the snow melts (Eagleson,1970), thereby affecting the climate system through changes in water and energy balances. In addition to local impacts, the continental snowpack over Eurasia can influence the large scale atmospheric circulation during winter (e.g., Li and Wang, 2014) or in spring (e.g., Broxton et al., 2017). Especially, the Eurasian autumn snow can affect upward-propagating stationary Rossby-wave activity, leading to stratospheric warming and weakening of stratospheric polar vortex and jet stream, which in turn emerges as a negative Arctic oscillation (AO)-like pattern at the surface during winter due to downward propagation through the troposphere. Its impact is shown in both observation and model experiments (e.g., Allen and Zender 2011; Cohen et al. 2007). Furthermore, the interannual variability of snow melting during the boreal spring season affects surface soil moisture in summer, which has important implications for heatwave development and emphasizing mechanisms through land-atmosphere interactions (Seo et al., 2020).

In the subseasonal to seasonal (S2S) timescales, land initial states are crucial components in the S2S timescale predictions due to the inherent memory that changes slowly for 1 to 2 months in the climate system (e.g., Derome et al. 2005; Chen et al., 2010; Seo et al., 2019). In particular, the realistic snow initial states contribute to improving S2S prediction skills, as proven in several modeling studies. For example, previous studies (Orsolini et al., 2013; Jeong et al., 2013) demonstrated a considerable enhancement in prediction skill of 2m air temperature up to a lead time of 1-2 months across certain regions of Eurasia and the Arctic during winter, depending on snow initialization. Moreover, other studies (Orsolini et al., 2016; Li et al., 2019) have revealed that wave activity propagating toward the stratosphere, influenced by snow initial conditions in climate models, can induce changes in the polar vortex and contribute to

78   the persistence of the North Atlantic Oscillation (NAO) and the AO. This emphasizes the

79   significance of snow initialization in climate models as an essential process for enhancing

80   prediction performance at the S2S timescales.

81   Snow states, i.e., snow water equivalent (SWE) used directly for hydrological analysis and

82   initial states of the model (Li et al., 2019; Gan et al., 2021), are generally provided from in-situ

83   observations data, remote-sensing retrievals from satellites, or numerical models such as the

84   land surface model (LSM) operated based on the observed atmospheric variables. For the in-

85   situ data snow depth (SD) measurements prevail, largely attributed to the challenges associated

86   with acquiring precise SWE data (Takala et al., 2011; De Rosnay et al., 2014). Surface synoptic

87   observations (SYNOP) serve as the principal source for SD measurements. The in-situ

88   measurements offer the most dependable snow information, yet they are characterized by

89   relatively coarse temporal and spatial resolutions, particularly within limited areas, due to the

90   spatial heterogeneity inherent in snow distribution. (Helmert et al., 2018; Meyal et al., 2020).

91   Satellite-derived observations using conical scanning microwave instruments may provide

92   spatially consistent data coverage across the globe. Cho et al. (2017) showed the SWE retrieval

93   results from two passive microwave sensors, the advanced microwave scanning radiometer 2

94   (AMSR2) and the special sensor microwave imager sounder (SSMIS). However, the

95   algorithms for SWE retrieval exhibit a degree of sensitivity to a variety of parameters such as

96   snow liquid water content and snow grain size distribution (De Rosnay et al., 2014). Hence,

97   satellite-based SWE data still have limitations in accuracy, especially under deep snow

98   conditions due to the limited penetration depth (Gan et al., 2021). On the other hand, satellite

99   retrieval can estimate snow cover accurately under clear sky conditions (Brubaker et al., 2009).

100   Model simulations obtained from LSMs and simple snow models can cover complete

101   spatiotemporal resolution but involve potentially large uncertainties due to the deficiencies in

102   the physical parameterizations and meteorological forcing data (Dirmeyer et al., 2006; Seo et

103   al., 2021).

104   Considering that snow observation dataset has its respective strengths as well as limitations,

105   data assimilation or other data fusion methods can prove to be beneficial for constructing snow

106   states such as reanalysis data (e.g., Brasnett, 1999; Dee et al., 2011; Meng et al., 2012; Pullen

107   et al., 2011; De Rosnay et al., 2014). For example, the snow analysis for the Canadian

108   Meteorological Center (CMC) utilizes a 2-dimensional optimal interpolation (2D-OI) scheme

109   with in-situ observations and the outputs from a simple snow model (Brown et al., 2003). The

110   National Centers for Environmental Prediction (NCEP) climate forecast system reanalysis

111   (CFSR) combines a multi-satellite-based interactive multi-sensor snow and ice mapping

112   system (IMS) as satellite-based snow cover retrieval and the outputs from the global snow

113   model of the Air Force Weather Agency (Meng et al., 2012). At the European Center for

114   Medium Weather Forecast (ECMWF), the ECMWF reanalysis (ERA)-Interim and ERA5 for

115   the snow analysis employ a Cressman interpolation and 2D-OI, respectively, with the IMS, in-

116   situ observation, and the results from a land surface model (Dee et al. 2011; De Rosnay et al.,

117   2014). The Japanese 55-year Reanalysis (JRA55) also utilizes the 2D-OI with in-situ

118   observation, satellite-based snow cover from SSMIS, and the results from an LSM (Kobayashi

119   et al., 2015). Given that the majority of the reanalysis datasets rely on snow depth

120   measurements, the SWE estimation is likely to introduce potential accuracy concerns when the

121   snow depth information is combined with the sow density calculations.

122   Climate prediction systems in operational centers such as the Meteorological Office (Met

123   Office) in the United Kingdom and the Korean Meteorological Administration (KMA) conduct

124   the snow initialization by utilizing the results of the operational global unified model (UM) and

125   the IMS snow cover, which solely indicates the presence of snow (Pullen et al., 2011), lacking

126   in its ability to reflect the physical quantity of it. The initialization at NCEP also performs a

127   similar approach using input data combined from IMS snow cover and results from the global

128 SD model (SNODEP; Meng et al., 2012). Furthermore, the snow initialization of ECMWF

129 employs optimal interpolation with a combination of results from the LSM, IMS snow cover,

130 and in-situ observation from SYNOP and national networks available on the GTS. However,

131 in regions where ground observations are unavailable, large errors may exist in the snow model

132 outputs due to uncertainties in atmospheric forcing and imperfect model parameterization

133 (Boone et al., 2004; Essery et al., 2009). Often, the snow processes parameterized in LSMs

134 rely on observed properties sampled in limited areas (Lim et al., 2022). In addition, as IMS

135 snow cover only identifies the presence of snow, the data assimilation with the satellite snow

136 cover only is not sufficient and inappropriate in constraining water and energy conservation.

137 Alternative methods that consider the physical quantity of snow are required for the snow

138 initialization.

139 One approach to mitigate the spatial discontinuity of ground observations is to use satellite-

140 derived SWE with wide spatial coverage and frequent temporal resolution. However, the SWE

141 retrievals from satellites still have considerable uncertainties (De Lannoy et al., 2010; Dawson

142 et al., 2018), which can arise from vegetation and terrain interference, sensor signal saturation,

143 snowfall amount, and simplifications in the underlying assumptions of the retrieval algorithms

144 (Liu et al., 2015). In particular, a region with heavy snow accumulation leads to a significant

145 underestimation of SWE due to the limitations in penetration depth from satellites (Gan et al.,

146 2021), so that satellite-derived SWE is not employed in the land initialization process. In

147 previous studies, various approaches have been attempted to improve SWE product

148 performance, such as combining satellite-derived SWE with ground observations (Pulliainen

149 et al., 2020), different satellite data sets (Gan et al., 2021), simple snow models (Dziubanski

150 and Franz, 2016), or LSMs (Kwon et al., 2017; Kumar et al., 2019). However, most previous

151 studies have focused on targeted regions with limited ground-based observations. Snow

152 initialization in global coverage using satellite-derived SWE remains a persistently challenging

153   task.

154   Therefore, this study developed an advanced SWE data assimilation framework with satellite

155   remote-sensing data using the local ensemble transform Kalman filter (LETKF) and the Joint

156   U.K. Land Environment Simulator (JULES) land model. While there are existing studies on

157   SWE data assimilation (e.g., Oaida et al., 2019; Smyth et al., 2020; Luojus et al., 2021), the

158   use of passive microwave observations based on the LETKF in this context is relatively rare

159   (e.g., Girotto et al., 2020). This approach constitutes an objective method that optimally

160   combines two previously unattempted incomplete data sources: the satellite SWE from the

161   Advanced Microwave Scanning Radiometer 2 (AMSR2) and the dynamically-balanced SWE

162   from the JULES land model forced by observed atmospheric fields. The estimated SWE data

163   exhibit better consistence by additionally using snow cover data from the IMS data. This

164   assimilation framework also enables the assessment of improvement as it provides insights into

165   the reasons behind the performance improvement based on the Kalman gain analysis that

166   measures the relative significance of the input data between the satellite and the land model

167   during the data assimilation cycle. The satellite data have demonstrated high reliability in the

168   transition regions of climatologically-shallow snow conditions (Gan et al., 2021), and these

169   regions are known as "hot spots" of strong atmosphere-land coupling through snow melting

170   and associated surface energy and water balance changes (Koster et al., 2004; Dirmeyer, 2011;

171   Huning and AghaKouchak, 2020). From these perspectives, it would be important to evaluate

172   the impact of satellites on the transition regions as well as on the deep accumulation regions

173   where accurate satellite retrievals are challenging. Furthermore, the benefits of assimilating

174   satellite retrievals in extremely high-temperature events, such as the case in April 2020 over

175   Eurasia, can be elucidated. In this regard, we expect that this snow data assimilation framework

176   with satellite-derived SWE can be significant in providing optimal snow initial states for

177   improving the S2S prediction by global climate models.

2. Data and model

2.1. Satellite data

The snow information including snow cover and SWE can be derived from satellite measurements offering global coverage and high temporal as well as spatial resolution. For data assimilation, this study uses SWE calculated from brightness temperature measurements obtained by the AMSR2 on board the Japanese Aerospace Exploration Agency (JAXA) global change observation mission-water (GCOM-W) satellite. This AMSR2 Unified Level-3 (L3) dataset offers daily estimation of SWE at 25 km resolutions from July 2012 to the present. AMSR2 has a sensor designed to detect microwave radiation naturally emitted from the surface and atmosphere, employing six frequency bands ranging from 6.9 to 89 GHz. Through this conical scanning mechanism, AMSR2 can acquire day and night datasets with nearly constant spatial resolution over more than 99% of the global coverage every two days. Comprehensive explanations of AMSR2 characteristics are available in Imaoka et al. (2010). AMSR2 is selected for the assimilation because it produces more accurate results by assimilating data from modern sensors (e.g., AMSR2) compared to data from conventional sensors (e.g., AMSR-E) (Cho et al., 2017).

The widely used multisensor–derived snow cover is IMS (e.g., Ramsay 1998; Helfrich et al., 2007) produced by NOAA the National Environmental Satellite Data and Information Service (NESDIS) for the Northern Hemisphere from February 2004 to the present at 4 km resolutions. This dataset is generated using various data products, including multi-satellite images and in-situ observations (U.S. National Ice Center, 2008). Since IMS provides binary (0: no snow or 1: snow covered) snow cover information, we transform the IMS snow cover at 4 km grids to the snow cover fraction (SCF) within a 50-km LSM grid by counting the snow pixel number with a value of 1. A 50-km LSM grid is declared as snow-covered when more than 50% of the 4km pixels within the grid are covered with snow. In this study, the application

204   of the assimilation process is determined based on IMS-based SCF, renowned for its superior

205   reliability (e.g., Brown et al., 2014). Further details will be described in Section 3.3.

206

207   **2.2. Reference data for SWE and SCF**

208   The CMC daily estimated SWE is used for verification. The SWE data is processed using

209   statistical interpolation between a background field derived from a simple snow model and in-

210   situ daily SD (Brown and Brasnett, 2010). In detail, this dataset utilizes optimal interpolation

211   methods to acquire spatial SD from the in-situ data, involving SYNOP, special aviation reports

212   from the World Meteorological Organization (WMO), and meteorological aviation reports

213   (METAR). In areas with scant in-situ data, a simple snow accumulation and melt model is

214   employed to create an optimal interpolation that estimates snowmelt and snowfall worldwide,

215   assuming the persistence of the snowpack mass between snowfall and melting events

216   (Brasnett, 1999). Although the average elevation of snow measurement stations used in CMC

217   is biased toward low elevations (< 400m), potentially causing relative negative biases at higher

218   elevations with heavy snow accumulation, the CMC dataset is often considered the premier

219   snow analysis accessible in the Northern Hemisphere (Su et al. 2010) and has still been widely

220   used to evaluate model outputs (e.g., Reichle et al., 2011; Reichle et al., 2017; Toure et al,

221   2018). Therefore, the SWE of CMC produced without the satellite-derived data is selected for

222   verification as an independent dataset for evaluating the assimilated analysis with remote

223   sensing snow retrievals. Since only daily SD analysis is provided in CMC, it is converted to

224   daily SWE based on the snow bulk density methods (e.g., Sturm et al., 2010). It is available

225   from 12 March 1998 to the present and offers comprehensive coverage of the entire Northern

226   Hemisphere with a horizontal resolution of 24 km. The SWE of CMC at its native horizontal

227   resolution is interpolated onto the LSM grid through local area averaging.

228

2.3. JULES LSM

229

230   This study utilizes the JULES LSM from the Met Office (Best et al., 2011), a component

231   land model of the global seasonal forecasting system version 6 (GloSea6) global, fully-coupled

232   atmosphere, ocean, land, and sea-ice model. The surface types (or snow tiles) in the JULES

233   LSM consist of four non-vegetated types: urban, land-ice, inland water, and bare soil, as well

234   as five vegetation functional types: C3 temperate grass, needleleaf trees, shrubs, C4 tropical

235   grass, and broadleaf trees. For each surface tile, a separate energy balance is computed, and the

236   average energy balance in the grid cells is determined by applying weights to the values of each

237   surface tile. Two schemes are used within JULES to represent surface snow (e.g., Best et al.,

238   2011; Burke et al., 2013). The simple method involves a zero-layer approach, which modifies

239   the top soil level without using explicit model layers to represent snow processes. The other is

240   the multi-layer approach which is more comprehensive, described in Best et al. (2011). In the

241   case of vegetated surfaces, snow can be separated into ground snow and canopy snow or stored

242   in a single effective reservoir. As both the zero-layer and multi-layer snow models provide

243   similar results under various conditions (Best et al., 2011), this study used the zero-layer snow

244   model with constant thermal conductivity and density for snow. Although the heat capacity of

245   snow is ignored, the bulk thermal conductivity in the surface layer is reduced as the thermal

246   conductivity of snow differs from that of the soil and the layer thickness increases. As long as

247   snow persists on the ground, the skin temperature cannot exceed 0°C, yet the heat flux utilized

248   for melting the snow is diagnosed as the residual in the surface energy balance. The melted

249   water is immediately drained from the snow, divided into runoff and soil infiltration, and liquid

250   water is not stored or frozen in the snow. A detailed description of the energy and water cycling

251   in the JULES LSM can be referenced in Best et al. (2011).

252   The prognostic variables (e.g., SWE) in the LSM are determined by meteorological forcing

253   variables such as 2-m air temperature, humidity, 10-m wind speed, precipitation, surface

254 pressure, and radiative fluxes. The 3-hourly, JRA55 reanalysis at 0.56° spatial resolution is

255 employed for the meteorological forcing variables, which is linearly interpolated to a 50 km

256 resolution of the LSM. The model background error needed for data assimilation is estimated

257 by JULES ensemble runs with perturbed initial and boundary conditions. Following the

258 previous studies (Reichle et al., 2008; Seo et al., 2021), meteorological forcing variables are

259 perturbed to account for the uncertainties in these variables, especially precipitation, downward

260 shortwave, and downward longwave. Perturbations are applied using additive adjustments

261 assuming a normal distribution for longwave radiation and multiplicative adjustments

262 following a log-normal distribution for shortwave radiation and precipitation, as guided by

263 previous studies (Seo et al., 2021). Here, the ensemble means of additional and multiplicative

264 perturbations are zero and one, respectively. The relationship between disturbed precipitation

265 and radiative flux ensures the physical consistency among atmospheric forcing variables

266 (Reichle et al., 2008). For instance, a negative anomaly in precipitation and downward

267 longwave-radiation is statistically linked to a positive anomaly of downward shortwave-

268 radiation. Detailed explanations regarding the perturbation of atmospheric forcings can be

269 found in Reichle et al. (2008).

270

3. Methodology

3.1. Bias correction

The discrepancy in SWE between remote sensing and LSMs often arises due to uncertainties in the model physics and forcing data and satellite retrievals. These uncertainties can lead to a significant discrepancy in SWE between model simulations and satellite remote-sensing retrievals, potentially degrading performance. In previous studies (e.g., Reichle and Koster, 2004; Seo et al., 2021), a scaling method of the nonlinear cumulative distribution function (CDF) matching is used to account for the systematic bias of soil moisture in the model backgrounds. However, unlike soil moisture, SWE presents varying characteristics in the CDF distribution across different regions, such as between high and low latitudes, thus requiring the estimation of distribution at each grid point. As a result, the insufficient sample size hinders the clear simulation of the CDF distribution, posing challenges in its application. To address this issue, we attempted to apply a simple and effective standard normal deviation scaling to satellite-derived SWE at each grid point, considering its potential use as initial conditions for JULES LSM-based climate models. Based on the climatology and standard deviation for the model and remote sensing retrievals, the scaled SWE (O_{new}) from the satellite can be derived from the following relation:

$$O_{new} = \left(\frac{O - \bar{O}}{\sigma_o} \times \sigma_m \right) + \bar{M} \tag{1}$$

where $\bar{O}(\sigma_o)$ and $\bar{M}(\sigma_m)$ indicate climatology (standard deviation) of remote sensing retrievals and the model, respectively. This approach has been widely utilized in observation-based land initialization and has proven to be effective (e.g., Koster et al., 2011; Jeong et al., 2013).

3.2. Data assimilation method

296

297 The snow assimilation is conducted based on the LETKF (e.g., Hunt et al., 2007), which is

298 utilized to combine remotely sensed retrievals with the LSM model outputs (a.k.a. backgrounds)

299 at each grid point to produce a snow analysis. Unlike variational data assimilation methods,

300 non-variational approaches (i.e., ensemble-based filters) characterize a probabilistic

301 representation with the spread of the ensemble serving as an estimate of forecast uncertainty.

302 LETKF has several advantages over other data assimilation methods. First, LETKF can

303 efficiently handle large datasets and high-dimensional state variables by localizing the

304 covariance matrix. This offers efficiency in parallel computing, making it suitable for real-time

305 forecasting and high-resolution data assimilation. In this study, the horizontal local patch size

306 and the localization length scale parameters are defined as 150 km and 30 km (Table 1),

307 respectively. This approach involves the weight function for the covariance localization within

308 the local patch centered at the analysis grid (e.g., Houtekamer and Mitchell, 2001; Hamill et

309 al., 2001). This function assigns larger errors to observations located farther away from the

310 center of the local patch, as proposed by Miyoshi and Yamane (2007), depending on the

311 Gaussian function. Secondly, the method utilizes model simulation ensembles to capture the

312 uncertainty in the initial states and background errors, which allows for a better representation

313 of the flow-dependent probability distribution of the state variables that vary in time and space.

314 Third, the LETKF employs an inflation parameter to adjust the ensemble spread, ensuring

315 realistic uncertainty estimation by accounting for background errors. The underestimation of

316 the analysis error covariance is typically issued by spatially and temporally constant boundary

317 conditions and observation errors and limited ensemble members. Based on the standardized

318 LETKF, this study applies a multiplicative covariance inflation of 20% of the spread of 24

319 member ensembles for each data assimilation cycle. Furthermore, the Kalman gain analysis

320 (Seo et al., 2021), which quantifies the ratio of the background error to the total error

321 (equivalent to the sum of the background and the observation error), is conducted. This analysis

322 serves to determine the weights assigned to assimilated observations in the analysis update

323 processes of the LETKF.

324

3.3. Snow data assimilation design

326 This study conducts the advanced daily cycle snow data assimilation experiment at each

327 grid point using the LETKF based on the satellite data and the JULES LSM model outputs

328 driven by 3-hourly JRA55 reanalysis atmospheric forcing. The snow assimilation processes are

329 illustrated in Fig. 1, with a more detailed description in Table 1. Since data assimilation is

330 conducted by considering the error of SWE in both the model and the observation, it is

331 important to accurately understand the observation and background errors to improve the

332 performance of data assimilation. The experiment calculates the background error from the 24

333 ensemble member spreads generated by perturbing atmospheric forcings such as longwave

334 radiation, shortwave radiation, and precipitation in JULES LSM, as provided in section 2.3.

335 Due to the absence of precise error estimates for AMSR2 SWE retrievals, the observation error

336 is conservatively prescribed as 10% of AMSR2 SWE for each grid compared to the previous

337 study utilizing AMSR2 SWE data (Lee et al., 2015), considering the general increase in the

338 errors during the snow accumulation period with the development of deep snowpack (Foster et

339 al., 2005; Cho et al., 2017). Here, the bias-corrected AMSR2 satellite data as described in

340 section 3.1 is used as the observation data, and the updated snow analysis state through data

341 assimilation becomes a new initial state for the next integration in JULES LSM (Fig. 1). In

342 addition, the analysis state of this method is calculated based on the IMS snow cover fraction

343 as follows (Fig. 1). If the SCF from IMS is 0, the snow analysis is set to zero; otherwise, it is

344 derived through data assimilation. The reason for this is due to the importance of the presence

345 or absence of snow in the climate system, as well as the high reliability of the IMS data (e.g.,

346   Brown et al., 2014). A background experiment of JULES LSM without satellite data

347   assimilation as a baseline (referred to hereafter as "Openloop") is also achieved by employing

348   the same ensemble perturbations, thereby measuring the skill improvement from the snow

349   analysis state through the assimilation of satellite-derived SWE and IMS SCF from satellite

350   and surface observations (referred to hereafter as "DA"). All experiments are conducted in

351   April from 2013 to 2020, which is one of the months with low snow performance in the LSM

352   when the snow begins to melt in the Northern Hemisphere (e.g., Toure et al., 2018; You et al.,

353   2020).

4. Results

4.1. Skill Verification

Figure 2 displays the climatological-mean SCF from the IMS multi-satellite data (Brown et al., 2014) and the differences from IMS for AMSR2, Openloop, JRA55, and DA for April 2013-2020. Here, the JRA55 SCF serves as a reference dataset for comparison with other reanalyses and is associated with meteorological forcing data used in the JULES land surface model. April is a season when the accumulated snow during the cold season begins to melt. This study defines the transitional region with a climatological-mean SWE of less than 16 mm as in previous studies (e.g., Gan et al., 2021), the boundary of these transition regions is represented by the black lines in Fig. 2. The transitional regions exhibit large variability in space and time, and they are mainly located at mid-latitudes. The SCF climatology patterns show negligible differences in high latitudes of heavy snow accumulation but noticeable differences in the transitional mid-latitude regions of less snow. SCF from JRA55 tends to be underestimated compared to IMS, whereas AMSR2 and Openloop tend to overestimate. There is a clear difference in SCF between AMSR2 and IMS satellite data. This study gives more credibility to IMS than AMSR2, as the former is based on multiple satellite data sources (e.g., Brown et al., 2014). As we used the IMS SCF to define the snow region to be assimilated by AMSR2 SWE, it is natural that DA shows better consistency with IMS and reduces overestimation biases in Openloop. Quantitatively, the root mean square differences (accuracy, defined in supplementary Table 1 as in previous study) for AMSR2, Openloop, JRA55, and DA with (from) IMS are 0.23 (0.91), 0.18 (0.91), 0.13 (0.93), and 0.13 (0.97), respectively, showing the best consistency in DA. The quantitative differences between DA and other experimental results are minor, but noticeable spatial discrepancies exist, particularly around transition regions.

The SWE climatology from AMSR2, Openloop, JRA55, and DA is also compared with

379   CMC as a reference in Fig. 3. The SWE derived from AMSR2 shows a significant

380   underestimation compared to CMC, particularly in the regions with heavy snow accumulation

381   at high latitudes. This is presumed to be due to limitations in satellite sensors detecting the

382   depth of snow (Gan et al., 2021). The SWE from JRA55 exhibits characteristics of

383   overestimation in high latitudes and underestimation in transitional regions. On the other hand,

384   the climatological SWEs from Openloop and DA exhibit higher correspondence to CMC, even

385   higher than JRA55. Specifically, DA demonstrates a higher agreement with CMC, despite the

386   marginal difference compared to Openloop. Quantitatively, the pattern correlation coefficients

387   (root mean square differences) for AMSR2, Openloop, JRA55, and DA with (from) CMC are

388   0.63 (80.7 kg/m^2), 0.80 (50.1 kg/m^2), 0.60 (100.8 kg/m^2), and 0.80 (49.9 kg/m^2), respectively.

389   Due to the application of standard deviation scaling to the satellite-derived SWE used in data

390   assimilation, the discrepancy in climatological SWE distributions between DA and Openloop

391   is deemed negligible. Despite its similarity to Openloop, DA with snow data assimilation

392   displays the relatively highest correlation and the smallest root mean square difference among

393   the datasets.

394   Next, we compare the temporal variation of SWE as measured by the Spearman rank

395   correlation coefficient with CMC, which is regarded as more appropriate than the Pearson

396   correlation coefficient for describing datasets containing nonlinearity and outliers such as snow

397   in both time and space. Figure 4 compares the distribution of correlation skills from AMSR2,

398   Openloop, JRA55, and DA. Openloop has a high performance in regions with heavy snow

399   accumulation but relatively low performance in transition regions with significant snow

400   changes. In contrast, the results from the AMSR2 satellite data represent poor performance in

401   high-latitude areas with heavy snow accumulation but high performance in transitional regions,

402   consistent with the previous studies (Gan et al., 2021). DA shows high performance not only

403   in high-latitude areas with heavy snow accumulation but also in transition regions. Even

404   compared to JRA55 used as the atmospheric forcing, DA performs better in temporal variation.

405   The quantitative results in the correlation in the Northern Hemisphere over 40°N (the transition

406   region) are 0.41 (0.54) for AMSR2, 0.61 (0.48) for Openloop, 0.58 (0.58) for JRA55, and 0.67

407   (0.61) for DA, respectively. The findings indicate that satellite retrievals offer additional value

408   in capturing temporal variations through data assimilation, indicating the benefit of

409   assimilating the AMSR2 SWE despite the overall lower performance of the satellite data itself.

410   The performance improvement by DA is also evident in the zonally-averaged correlation

411   coefficient shown in Fig. 5. The AMSR2 satellite data shows higher performance than

412   Openloop in the transition region around latitude 45 °N-55 °N, although performance sharply

413   decreases with increasing snow accumulation. Openloop indicates gradually increasing

414   performance as the latitude increases, with the highest performance at around 60°N. DA

415   denotes superior performance across the Northern Hemisphere, especially in the mid-latitude

416   transition region than AMSR2 or JRA55. An exception is for 35-40°N in the Tibetan Plateau,

417   where JRA55 used in-situ observations. The results suggest that the developed snow data

418   assimilation system represents well not only the transitional regions but also the regions with

419   high snow accumulation that are difficult to detect by satellite.

420   Figure 6 presents the Spearman rank correlation depending on the SWE amount in the

421   Northern Hemisphere. AMSR2 exhibits higher performance than Openloop for SWE up to 16

422   mm. However, the performance of AMSR2 sharply declines beyond that threshold, and

423   Openloop shows a better performance. Consistent with the results illustrated in Figs. 4 and 5,

424   DA demonstrates superior performance compared to others. Note that DA performs

425   significantly better in the transition region of less than 16 mm of SWE. Considering that the

426   area below 16 mm of SWE accounts for approximately 53% of the entire area of the Northern

427   Hemisphere(as shown in the pie chart in Fig. 6), the data assimilation impact is identifiable,

428   and it can contribute substantially to the increase in the prediction skill through improving the

429   simulation of the albedo changes and surface energy balance.

430   Consistent with the description in Section 3.3, this study considers an algorithm based on

431   the highly reliable IMS satellite SCF data to identify the presence of snow and determine the

432   assimilation process. Therefore, a further sensitivity test is conducted to investigate the

433   influence of incorporating IMS data in snow assimilation. Figure 7 compares the correlation

434   differences between Openloop and the data assimilation result employing both AMSR2 and

435   IMS (DA), as well as the data assimilation result utilizing solely AMSR2 and excluding IMS

436   (hereafter referred to as DA_AMSR2). The results obtained from the snow assimilation show

437   the improvements in the transitional regions where AMSR2 denotes a better agreement with

438   the observations compared to Openloop. Notably, the skill is enhanced significantly in DA by

439   incorporating the IMS SCF. DA exhibits inferior performance compared to Openloop in certain

440   exceptional cases, which may be attributed to discrepancies in snow identification between the

441   CMC observations used for correlation and the IMS data utilized for data assimilation.

442   Moreover, the performance of SWE improves even when only AMSR2 is used, but

443   incorporating IMS leads to a substantial improvement in the transitional regions. This implies

444   that IMS has a positive influence on the snow data assimilation.

445

446   **4.2 Kalman gain analysis**

447   In order to better understand the skill enhancement through snow assimilation of satellite

448   data, this section examines the Kalman gain. Figure 8 illustrates the spatial distribution of

449   observation error, model background error, and the Kalman gain for SWE. A high value of the

450   Kalman gain denotes that the assimilated result is closer to the AMSR2 observation than the

451   model background. The Kalman gain is large when the background error becomes large, or the

452   observation error is small. As this study specifies the observation error as a conservative 10%

453   of SWE compared to the previous study (Lee et al., 2015), the observation error basically

454   follows the distribution similar to the climatological-mean values. The background errors,

455   originating from the 24 ensemble members, have higher values in high-latitude regions and

456   mid-latitude regions. Data assimilation methods such as LETKF used in this study often face

457   challenges in accurately representing background errors when the ensemble spread is

458   insufficient. Generally, the magnitude of ensemble spread is frequently compared to the root

459   mean square error (RMSE). The ensemble spread in this study demonstrates a sufficiently valid

460   magnitude in comparison with the RMSE, as illustrated in SFig. 1, indicating that it is well

461   estimated. Moreover, the standardized distribution of SWE among the ensemble members

462   exhibits a quasi-Gaussian distribution centered around zero, with the transition region showing

463   a closer resemblance to a standardized Gaussian distribution (SFig. 4). In the spatial

464   distribution of Kalman gain in Fig. 8c, significant performance improvement is observed in

465   transition regions, where Kalman gains exhibit larger values. However, in high-latitude areas

466   with substantial snow accumulation, there is a tendency for Kalman gain to have lower values.

467   These findings agree well with the bar graph in Fig. 9, which illustrates the Kalman gain as a

468   function of SWE amount. In the region encompassing the transition region with SWE amounts

469   below 20 mm, the Kalman gain displays the highest values, particularly exceeding 0.8. As the

470   SWE amount increases, the Kalman gain decreases, with a significant decline observed when

471   the SWE amount reaches 80-100 mm or higher. Furthermore, in the areas where DA denotes

472   improved skill compared to Openloop, the Kalman gain shows values generally above 0.7. In

473   contrast, relatively lower values below 0.5 are observed in the areas with decreased skill. This

474   indicates that in the dominant areas of performance improvement, including the transition

475   region, the background error is significantly larger than the observation error, emphasizing the

476   substantial influence of observations in data assimilation. It is found that accurate remote

477   sensing retrievals are well reflected in regions with high uncertainty in the LSM through the

478   snow data assimilation system, leading to performance improvement.

4.3 Validation of the SWE for the extreme event

In April 2020, Siberia experienced a record-breaking heatwave with the highest observed average temperature. This section investigates the potential benefits of snow assimilation using satellite data for the case of the 2020 Siberian heatwave. Previous studies have identified the strong polar vortex accompanied by the AO amplification during winter as a major cause of the cold Eurasian region (Overland and Wang, 2021). Additionally, it has been revealed that the occurrence of high temperatures in the Siberian region is found to be closely associated with large-scale atmospheric waves in the upper atmosphere over the Eurasian region originating from the Atlantic (De Angelis et al., 2023). As a result, remarkable snow melting occurred due to the high surface temperature over the Siberian region in April 2020, leading to extremely low values of SWE and SCF as depicted in SFig. 2. This is consistent with previous studies reporting a significant snow depletion in 2020 in the region (Gloege et al., 2022). Especially, as shown in Fig. 10, significant negative anomalies in SWE and SCF are predominant over the transition region. Substantial snow melt can contribute to record-breaking heatwaves through albedo feedback and changes in the ratio of the latent and sensible heat fluxes from the exposed surface, coupled with favorable atmospheric circulation patterns (Collow et al., 2022). Collow et al. (2022) demonstrated that the exposed surface contributed to up to 20% of the temperature anomaly over Siberia in spring 2020. This implies the importance of realistic snow initial states in the global coupled model forecasts. For the Siberian region with extreme high-temperature events marked by the red box in Fig. 10, DA shows a better agreement with the extremely dry snow conditions, especially in the transitional region, compared to the Openloop. These results are evident when considering the observation-to-model ratio in that region. The percentage of CMC (IMS) is 83% (78%) for Openloop and 93% (89%) for DA, indicating that DA with snow data assimilation based on satellite data effectively replicates the observed snow depletion in comparison with Openloop. Similarly to

504   the 2020 case, we obtained another significant case in 2014 compared to Openloop, as shown

505   in SFig. 3. Such extremely dry snow conditions can provide significant heatwave events in the

506   following months.

507

508

509

510

511

512

5. Conclusions and discussion

The advanced SWE data assimilation is developed in this study with the LETKF data assimilation method and the JULES LSM. The system assimilates snow water equivalent retrievals from AMSR2 and IMS snow cover. This constitutes an objective way to optimally combine two imperfect data sources for SWE from satellite remote sensing data and the land surface model simulation forced by observed atmospheric data. This study shows that the satellite-derived SWE has limitations in penetrating deep snow and exhibited much discrepancy from the SWE obtained from the Openloop LSM simulations. The SWE assimilation in this study proves the beneficial impacts of using satellite snow data, maintaining better analysis quality by dynamically balancing the errors from the satellite observations and the model background states.

It is found that the simulation from Openloop as a baseline shows superior performance in high-latitude regions with heavy snow accumulation but relatively inferior performance in transition regions with much variation of snow in space and time. Contrastingly, the AMSR2 satellite data represent poor performance in high-latitude regions but exhibit relatively better performance in the transition regions. The SWE from the LETKF data assimilation consistently exhibits better performance in capturing the climatology and temporal variation compared to other results. It specifically improves the analysis in the mid-latitude transition regions that cover approximately 53% of the entire areas of the Northern Hemisphere. It is found that the model background errors estimated from the ensemble spread are significantly larger than the observation errors, thereby reflecting satellite information more in those regions. The LETKF data assimilation also proves reliable representation in the heavy snow regions due to low ensemble spread and large uncertainty in the satellite retrievals. Moreover, during the record-breaking heatwave in Siberia in April 2020, the remarkable snow depletion observed due to high surface temperatures is more realistically reproduced by our snow analysis compared to

538   the Openloop.

539   This snow data assimilation framework is anticipated to contribute to a more precise

540   prediction of atmospheric conditions by realistically capturing the interaction between the

541   atmosphere and land, given the substantial influence of SWE on energy and water balance at

542   the interface of the atmosphere and land. Specifically, this applies to the transitional regions

543   with high spatial and temporal variability. The long-term analysis of snow manifests a

544   pronounced variability in the continental interior at the interannual timescales, potentially

545   improving the prediction of extreme heatwave events by global climate models. This study

546   used the gridded CMC data from in-situ observations for the validation. Although existing

547   snow data are subject to much uncertainty and limitations, we expect to obtain comparable

548   conclusions and significant benefits of optimally combining satellite SWE data and the LSM

549   model simulations through LETKF data assimilation method.

550   The quality of the observation is crucial in the data assimilation system. Satellite-derived

551   snow cover exhibits a significantly higher accuracy compared to other data sources, while SWE

552   has restricted performance due to the limitations of penetration depth by satellite sensors and

553   relies heavily on estimation algorithms. Due to these problems, most previous studies and

554   operational centers primarily depend on satellite-derived snow cover for snow initialization.

555   However, the findings from this study highlighted the beneficial impacts of using satellite-

556   derived SWE, particularly in the rapidly changing transition areas, to find out which variable

557   is more important in closing surface energy and water balance changed by snow. Nevertheless,

558   areas of significance in large-scale circulation, such as the Tibetan region, which experiences

559   significant uncertainty and degraded performance in satellite data, do not exhibit substantial

560   data assimilation effects. As the performance of SWE derived from various satellites continues

561   to advance, these issues will be discussed more.

562

Key words

Snow data assimilation, AMSR2, LETKF, snow water equivalent, JULES LSM

Data availability.

The AMSR2 SWE and IMS SC were obtained from https://n5eil01u.ecs.nsidc.org/AMSA/AU_DySno.001/ and https://noaadata.apps.nsidc.org/NOAA/G02156/, respectively. The CMC SWE was collected from https://daacdata.apps.nsidc.org/pub/DATASETS/nsidc0447_CMC_snow_depth_v01/. The snow-assimilated results and land surface variables from the LSM offline simulation may be requested from the authors.

Author contributions.

LJL conceived the project, designed the study, developed the snow assimilation system, wrote the paper, and made the figures. LMI provided advice on the methods, project design, and review and editing of the manuscript. TSL helped with the experiment with the land surface model. SEK helped with the data assimilation method based on LETKF. LYK provided advice on snow satellite data and the sensitivity methods. All authors contributed to the writing of the paper by providing comments and feedback.

Competing interests.

The contact author has declared that none of the authors has any competing interests.

Acknowledgements

This work was funded by the Korea Meteorological Administration Research and Development Program under Grant (RS-2024-00403698). ES was supported by Learning & Academic research institution for Master's·PhD students, and Postdocs (LAMP) Program of the National Research Foundation of Korea (NRF) grant funded by the Ministry of Education (RS-2023-000301702). We thank the supercomputing resources of the UNIST Supercomputing Center.

Reference

Allen, R.J., Zender, C.S.: Forcing of the Arctic Oscillation by Eurasian snow cover. J. Clim. 24 (24), 6528-6539, 2011.

Best, M.J., Pryor, M., Clark, D.B., Rooney, G.G., Essery, R., Ménard, C.B., Edwards, J.M., Hendry, M.A., Porson, A., Gedney, N., Mercado, L.M., Sitch, S., Blyth, E., Boucher, O., Cox, P.M., Grimmond, C.S.B., Harding, R.J.: The Joint UK Land Environment Simulator (JULES), model description–Part 1: energy and water fluxes. Geosci. Model Dev. 4, 677–699, 2011.

Boone, A., Habets, F., Noilhan, J., Clark, D., Dirmeyer, P., Fox, S., Gusev, Y., Haddeland, I., Koster, R., Lohmann, D., Mahanama, S., Mitchell, K., Nasonova, O., Niu, G.Y., Pitman, A., Polcher, J., Shmakin, A., Tanaka, K., van den Hurk, B., Ve´ rant, S., Verseghy, D., Viterbo, P., Yang, Z.L.: The Rhone-Aggregation land surface scheme intercomparison project: an overview. J. Clim. 17, 187–208, 2004.

Brasnett, B.: A global analysis of snow depth for numerical weather prediction. J. Appl. Meteorol. 38 (6), 726–740, 1999.

Brown, L.C., Howell, S.E., Mortin, J., Derksen, C.: Evaluation of the Interactive Multisensor Snow and Ice Mapping System (IMS) for monitoring sea ice phenology. Remote Sens. Environ. 147, 65–78. doi: 10.1016/j.rse.2014.02.012, 2014.

Brown, R.D., Brasnett, B.: Canadian Meteorological Centre (CMC) Daily Snow Depth Analysis Data. NASA National Snow and Ice Data Center Distributed Active Archive Center, Boulder, Colorado, USA. https://doi.org/10.5067/ W9FOYWH0EQZ3, 2010.

Brown, R.D., Brasnett, B., Robinson, D.: Gridded North American monthly snow depth and snow water equivalent for GCM evaluation. Atmos.–Ocean, 41, 1–14, 2003.

Broxton, P.D., Zeng, X., Dawson, N.: The impact of a low bias in snow water equivalent initialization on CFS seasonal forecasts. J. Clim. 30 (21), 8657–8671. https://doi.org/10.1175/JCLI-D-17-0072.1, 2017.

Brubaker, K., Pinker, R., Deviatova, E.: Evaluation and comparison of MODIS and IMS snow-cover estimates for the continental United States using station data. J. Hydrometeorol. 6, 1002–1017, 2009.

Burke, E. J., Dankers, R., Jones, C. D., and Wiltshire, A. J.: A retrospective analysis of pan Arctic permafrost using the JULES land surface model, Clim. Dynam., 41, 1025–1038, https://doi.org/10.1007/s00382-012-1648-x, 2013.

Chen, M., Wang, W., Kumar, A.: Prediction of monthly-mean temperature: The roles of atmospheric and land initial conditions and sea surface temperature J. Clim. 23(3), 717-725, 2010.

Cho, E., Tuttle, S.E., Jacobs, J.M.: Evaluating consistency of snow water equivalent retrievals from passive microwave sensors over the north central US: SSM/I vs. SSMIS and AMSR-E vs. AMSR2. Remote Sens. 9(5), 465, 2017.

Cohen, J., Barlow, M., Kushner, P. J., Saito, K.: Stratosphere–troposphere coupling and links with eurasian land surface variability. J. Clim. 20(21), 5335–5343. https://doi.org/10.1175/2007jcli1725.1, 2007.

633 Collow, A.B.M., Thomas, N.P., Bosilovich, M.G., Lim, Y.K., Schubert, S.D., Koster, R.D.: Seasonal variability
634   in the mechanisms behind the 2020 Siberian heatwaves. J. Clim. 35(10), 3075-3090, 2022.

635 Dawson, N., Broxton, P., Zeng, X.: Evaluation of remotely sensed snow water equivalent and snow
636   cover extent over the contiguous United States. J. Hydrometeorol. 19 (11), 1777–1791.
637   https://doi.org/10.1175/JHM-D-18-0007.1, 2018.

638 De Angelis, A.M., Schubert, S.D., Chang, Y., Lim, Y.K., Koster, R.D., Wang, H., Marquardt Collow, A.B.:
639   Dynamical Drivers of the Exceptional Warmth over Siberia during the Spring of 2020. J.
640   Clim. 36(15), 4837-4861, 2023.

641 De Lannoy, G.J.M., Reichle, R.H., Houser, P.R., Arsenault, K.R., Verhoest, N.E.C., Pauwels, V.R.N.: Satellite-
642   scale snow water equivalent assimilation into a high-resolution land surface model. J.
643   Hydrometeorol. 11 (2), 352–369. https://doi. org/10.1175/2009JHM1192.1, 2010.

644 De Rosnay, P., Balsamo, G., Albergel, C., Muñoz-Sabater, J., Isaksen, L. Initialisation of land surface
645   variables for numerical weather prediction. Surv. Geophys. 35, 607-621, 2014.

646 Dee, D., Uppala, S., Simmons, A., Berrisford, P., Poli, P., Kobayashi, S., Andrae, U., Balsameda, M.,
647   Balsamo, G., Bauer, P., Bechtold, P., Beljaars, A.C.M., van de Berg, L., Bidlot, J., Bormann, N.,
648   Delsol, C., Dragani, R., Fuentes, M., Geer, A.J., Haimberger, L., Healy, S.B., Hersbach, H., Hólm,
649   E.V., Isaksen, L., Kållberg, P., Köhler, M., Matricardi, M., McNally, A.P., Monge-Sanz, B.M.,
650   Morcrette, J.-J., Park, B.-K., Peubey, C., de Rosnay, P., Tavolato, C., Thépaut, J.-N., Vitart, F.: The
651   ERA-Interim reanalysis: Configuration and performance of the data assimilation system. Q.
652   J. R. Meteorol. Soc. 137, 553–597, 2011.

653 Derome J, Lin H, Brunet, G.: Seasonal forecasting with a simple general circulation model: Predictive
654   skill in the AO and PNA. J. Clim., 15, 597–609, 2005.

655 Dirmeyer, P.A.: The terrestrial segment of soil moisture–climate coupling. Geophys. Res. Lett. 38(16),
656   2011.

657 Dirmeyer, P.A., Gao, X., Zhao, M., Guo, Z., Oki, T., Hanasaki, N.: The Second Global Soil Wetness
658   Project (GSWP-2): Multi-model analysis and implications for our perception of the land
659   surface. Bull. Amer. Meteor. Soc. 87, 1381–1397, 2006.

660 Dutra, E., Schär, C., Viterbo, P., Miranda, P. M.: Land-atmosphere coupling associated with snow
661   cover. Geophys. Res. Lett. 38 (15) , 2011.

662 Dziubanski, D.J., Franz, K.J.: Assimilation of AMSR-E snow water equivalent data in a spatially-lumped
663   snow model. J. Hydrol. 540, 26–39. https://doi.org/10.1016/j.jhydrol.2016.05.046, 2016.

664 Essery, R.L.H., Rutter, N., Pomeroy, J., Baxter, R., Stahli, M., Gustafsson, D., Barr, A., Bartlett, P., Elder,
665   K.: SNOWMIP2: an evaluation of forest snow process simulations. Bull. Amer. Meteor. Soc.
666   90, 1120–1135, 2009.

667 Eagleson, P.S.: Dynamic Hydrology, McGraw-Hill, 1970

668 Foster, J.L., Sun, C., Walker, J.P., Kelly, R., Chang, A., Dong, J., Powell, H.: Quantifying the uncertainty
669   in passive microwave snow water equivalent observations. Remote Sens. Environ. 94, 187–
670   203, 2005.

671 Gan, Y., Zhang, Y., Kongoli, C., Grassotti, C., Liu, Y., Lee, Y. K., Seo, D. J.: Evaluation and blending of

672   ATMS and AMSR2 snow water equivalent retrievals over the conterminous United
673   States. Remote Sens. Environ. 254, 112280, 2021.

674 Girotto, M., Musselman, K. N., and Essery, R. L. H.: Data Assimilation Improves Estimates of Climate-
675   Sensitive Seasonal Snow, Current Climate Change Reports, 6, 81–94,
676   https://doi.org/10.1007/s40641-020-00159-7, 2020.

677 Gloege, L., Kornhuber, K., Skulovich, O., Pal, I., Zhou, S., Ciais, P., Gentine, P.: Land-Atmosphere Cascade
678   Fueled the 2020 Siberian Heatwave. AGU Advances, 3 (6), e2021AV000619, 2022.

679 Hamill, T.M., Whitaker, J.S., Snyder, C.: Distance-dependent filtering of background error covariance
680   estimates in an ensemble Kalman filter. Mon. Weather Rev. 129, 2776–2790, 2001.

681 Helfrich, S.R., McNamara, D., Ramsay, B.H., Baldwin, T., Kasheta, T.: Enhancements to, and forthcoming
682   developments in the interactive multisensor snow and ice mapping system (IMS). Hydrol.
683   Process. 21 (12), 1576–1586. https:// doi.org/10.1002/hyp.6720, 2007.

684 Helmert, J., Şensoy Şorman, A., Montero, R.A., De Michele, C., De Rosnay, P., Dumont, M., Finger, D.,
685   Lange, M., Picard, G., Potopová, V., et al.: Review of Snow Data Assimilation Methods for
686   Hydrological, Land Surface, Meteorological and Climate Models: Results from a COST
687   HarmoSnow Survey. Geoscience, 8 (12), 489, 2018.

688 Houtekamer, P.L., Mitchell, H.L.: A sequential ensemble Kalman filter for atmospheric data
689   assimilation. Mon. Weather Rev. 129, 123–137, 2001.

690 Huning, L.S., AghaKouchak, A.: Global snow drought hot spots and characteristics. Proc. Natl. Acad.
691   Sci. 117(33), 19753-19759, 2020.

692 Hunt, B.R., Kostelich, E.J., Szunyogh, I.: Efficient data assimilation for spatiotemporal chaos: a local
693   ensemble transform Kalman filter. Phys. D Nonlinear Phenom. 230, 112–126, 2007.

694 Imaoka, K., Kachi, M., Kasahara, M., Ito, N., Nakagawa, K., Oki, T.: Instrument performance and
695   calibration of AMSR-E and AMSR2. Int. Arch. Photogramm. Remote. Sens. Spat. Inf. Sci. 38
696   (8), 13–16, 2010.

697 Jeong, J.H., Linderholm, H.W., Woo, S.H., Folland, C., Kim, B.M., Kim, S.J., Chen, D.: Impacts of snow
698   initialization on subseasonal forecasts of surface air temperature for the cold season. J.
699   Clim. 26 (6), 1956-1972, 2013.

700 Kobayashi, S., Ota, Y., Harada, Y., Ebita, A., Moriya, M., Onoda, H., Onogi, K., Kamahori, H., Kobayashi,
701   C., Endo, H.: The JRA-55 reanalysis: general specifications and basic characteristics. J.
702   Meteorol. Soc. Jpn. Ser. II 93, 5–48, 2015.

703 Koster, R.D., Dirmeyer, P.A., Guo, Z., Bonan, G., Chan, E., Cox, P., Gordon, C.T., Kanae, S., Kowalczyk,
704   E., Lawrence, D., Liu, P., Lu, C.H., Malyshev, S., McAvaney, B., Mitchell, K., Mocko, D., Oki,
705   T., Oleson, K., Pitman, A., Sud, Y.C., Taylor, C.M., Verseghy, D., Vasic, R., Xue, Y., Yamada,
706   T., GLACE Team: Regions of strong coupling between soil moisture and
707   precipitation. Science, 305 (5687), 1138–
708   1140, https://doi.org/10.1126/science.1100217, 2004.

709 Koster, R.D., Mahanama, S., Yamada, T., Balsamo, G., Berg, A., Boisserie, M., Dirmeyer, P., Doblas-Reyes,
710   F., Drewitt, G., Gordon, C.: The second phase of the global land–atmosphere coupling

experiment: soil moisture contributions to subseasonal forecast skill. J. Hydrometeorol. 12, 805–822, 2011.

Kumar, S.V., Jasinski, M., Mocko, D.M., Rodell, M., Borak, J., Li, B., Beaudoing, H.K., Peters-Lidard, C.D.: NCA-LDAS land analysis: development and performance of a multisensor, multivariate land data assimilation system for the national climate assessment. J. Hydrometeorol. 20 (8), 1571–1593. https://doi.org/10.1175/JHM-D- 17-0125.1, 2019.

Kwon, Y., Yang, Z.-L., Hoar, T.J., Toure, A.M.: Improving the radiance assimilation performance in estimating snow water storage across snow and land-cover types in North America. J. Hydrometeorol. 18 (3), 651–668. https://doi.org/10.1175/JHM-D-16-0102.1, 2017.

Lee, Y.K., Kongoli, C., Key, J.: An in-depth evaluation of heritage algorithms for snow cover and snow depth using AMSR-E and AMSR2 measurements. J. Atmos. Ocean. Technol. 32(12), 2319-2336, 2015.

Li, F., Orsolini, Y.J., Keenlyside, N., Shen, M.L., Counillon, F., Wang, Y.G.: Impact of snow initialization in subseasonal-to-seasonal winter forecasts with the Norwegian Climate Prediction Model. J. Geophys. Res. Atmos. 124 (17-18), 10033-10048, 2019.

Li, F., Wang, H.: Autumn Eurasian snow depth, autumn Arctic sea ice cover and East Asian winter monsoon. Int. J. Climatol. 34(13), 3616-3625, 2014.

Lim, S., Gim, H.J., Lee, E., Lee, S., Lee, W.Y., Lee, Y.H., Cassardo C., Park, S.K.: Optimization of snow-related parameters in the Noah land surface model (v3. 4.1) using a micro-genetic algorithm (v1. 7a). Geosci. Model Dev. 15(22), 8541-8559, 2022.

Liu, Y., Peters-Lidard, C.D., Kumar, S.V., Arsenault, K.R., Mocko, D.M.: Blending satellite-based snow depth products with in situ observations for streamflow predictions in the upper Colorado River basin. Water Resour. Res. 51 (2), 1182–1202. https://doi.org/10.1002/2014WR016606, 2015.

Luojus, K., Pulliainen, J., Takala, M., Lemmetyinen, J., Mortimer, C., Derksen, C., Mudryk, L., Moisander, M., Hiltunen, M., Smolander, T., Ikonen, J., Cohen, J., Salminen, M., Norberg, J., Veijola, K., and Venäläinen, P.: GlobSnow v3.0 Northern Hemisphere snow water equivalent dataset, Sci. Data, 8, 163, https://doi.org/10.1038/s41597-021-00939-2, 2021.

Meng, J., Yang, R., Wei, H., Ek, M., Gayno, G., Xie, P., Mitchell, K.: The land surface analysis in the NCEP climate forecast system reanalysis. J. Hydrometeorol. doi:10.1175/JHM-D-11-090.1, 2012.

Meyal, A.Y., Versteeg, R., Alper, E., Johnson, D., Rodzianko, A., Franklin, M., Wainwright, H.: Automated cloud based long short-term memory neural network based SWE prediction. Front. Water, 2, 574917, 2020.

Miyoshi, T., Yamane, S.: Local ensemble transform Kalman filtering with an AGCM at a T159/L48 resolution. Mon. Weather Rev. 135, 3841–3861, 2007.

Oaida, C. M., Reager, J. T., Andreadis, K. M., David, C. H., Levoe, S. R., Painter, T. H., Bormann, K. J., Trangsrud, A. R., Girotto, M., and Famiglietti, J. S.: A High-Resolution Data Assimilation Framework for Snow Water Equivalent Estimation across the Western United States and

Validation with the Airborne Snow Observatory, J. Hydrometeorol., 20, 357–378, https://doi.org/10.1175/JHM-D-18-0009.1, 2019.

Orsolini, Y.J., Senan, R., Balsamo, G., Doblas-Reyes, F.J., Vitart, F., Weisheimer, A., Carrasco, A., Benestad, R.E.: Impact of snow initialization on sub-seasonal forecasts. Clim. Dyn. 41, 1969-1982, 2013.

Orsolini, Y.J., Senan, R., Vitart, F., Weisheimer, A., Balsamo, G., Doblas-Reyes, F.: Influence of the Eurasian snow on the negative North Atlantic Oscillation in subseasonal forecasts of the cold winter 2009/10. Clim. Dyn. 47(3-4), 1325–1334. https://doi.org/10.1007/s00382-015-2903-8, 2016.

Overland, J. E., Wang, M.: The 2020 Siberian heat wave. Int. J. Climatol. 41, E2341-E2346, 2021.

Pullen, S., Jones, C., Rooney, G.: Using satellite-derived snow cover data to implement a snow analysis in the met office NWP model. J. Appl. Meteorol. 50, 958–973. doi:10.1175/2010JAMC2527.1, 2011.

Pulliainen, J., Luojus, K., Derksen, C., Mudryk, L., Lemmetyinen, J., Salminen, M., Ikonen, J., Takala, M., Cohen, J., Smolander, T., Norberg, J.: Patterns and trends of Northern Hemisphere snow mass from 1980 to 2018. Nature, 581 (7808), 294–298. https://doi.org/10.1038/s41586-020-2258-0, 2020.

Ramsay, B.H.: The interactive multisensor snow and ice mapping system. Hydrol. Process. 12 (10-11), 1537–1546, 1998.

Reichle, R.H.: Data assimilation methods in the Earth sciences. Adv. Water Resour. 31, 1411–1418, 2008.

Reichle, R.H., Draper, C.S., Liu, Q., Girotto, M., Mahanama, S.P, Koster, R.D., De Lannoy, G.J.: Assessment of MERRA-2 land surface hydrology estimates. J. Clim. 30 (8), 2937-2960, 2017.

Reichle, R.H., Koster, R.D.: Bias reduction in short records of satellite soil moisture. Geophys. Res. Lett. 31, 2004.

Reichle, R.H., Koster, D., De Lannoy, G.J.M., Forman, B.A., Liu, Q., Mahanama, S.P.P., Toure, A.M.: Assessment and Enhancement of MERRA Land Surface Hydrology Estimates. J. Clim. 24, 6322–6338, 2011.

Seo, E., Lee, M.I., Jeong, J.H., Koster, R.D., Schubert, S.D., Kim, H.M., Kim, D.H., Kang H.S., Kim, H.K., MacLachlan, C., Scaife, A.A.: Impact of soil moisture initialization on boreal summer subseasonal forecasts: mid-latitude surface air temperature and heat wave events. Clim. Dyn. 52, 1695-1709, 2019.

Seo, E., Lee, M.I., Reichle, R.H.: Assimilation of SMAP and ASCAT soil moisture retrievals into the JULES land surface model using the Local Ensemble Transform Kalman Filter. Remote Sens. Environ. 253, 112222, 2021.

Seo, E., Lee, M.I., Schubert, S.D., Koster, R.D., Kang, H.S.: Investigation of the 2016 Eurasia heat wave as an event of the recent warming. Environ. Res. Lett. 15(11), 114018, 2020.

Shlyaeva, A., Tolstykh, M., Mizyak, V., Rogutov, V.: Local ensemble transform Kalman filter data assimilation system for the global semi-Lagrangian atmospheric model. Russ. J. Numer. Anal. Math. Model. 28(4), 419-442, 2013.

789 Smyth, E. J., Raleigh, M. S., and Small, E. E.: Improving SWE Estimation With Data Assimilation: The
790   Influence of Snow Depth Observation Timing and Uncertainty, Water Resour. Res., 56,
791   e2019WR026853, https://doi.org/10.1029/2019WR026853, 2020.

792 Sturm, M., Taras, B., Liston, G.E., Derksen, C., Jonas, T., Lea, J.: Estimating snow water equivalent using
793   snow depth data and climate classes. J. Hydrometeor. 11, 1380–1394, 2010.

794 Su, H., Yang, Z.-L., Dickinson, R.E., Wilson, C.R., Niu, G.-Y.: Multisensor snow data assimilation at the
795   continental scale: The value of gravity recovery and climate experiment terrestrial water
796   storage information. J. Geophys. Res., 115, D10104, doi:10.1029/2009JD013035, 2010.

797 Takala, M., Luojus, K., Pulliainen, J., Derksen, C., Lemmetyinen, J., Karna, J.P., Koskinen, J., Bojkov, B.:
798   Estimating northern hemisphere snow water equivalent for climate research through
799   assimilation of space-borne radiometer data and ground-based measurements. Remote
800   Sens. Environ. 115:3517–3529, 2011.

801 Thomas, J.A., Berg, A.A., Merryfield, W.J.: Influence of snow and soil moisture initialization on sub-
802   seasonal predictability and forecast skill in boreal spring. Clim. Dyn. 47 (1), 49-65, 2016.

803 Toure, A.M., Luojus, K., Rodell, M., Beaudoing, H., Getirana, A.: Evaluation of simulated snow and
804   snowmelt timing in the Community Land Model using satellite-based products and
805   streamflow observations. J. Adv. Model. Earth Syst. 10(11), 2933-2951, 2018.

806 U.S. National Ice Center: IMS daily Northern Hemisphere snow and ice analysis at 1 km, 4 km, and
807   24 km resolutions, version 3. Boulder, Colorado, USA. NSIDC: National Snow and Ice Data
808   Center, accessed: 18 Aug 2022, https://doi.org/10.7265/N52R3PMC, 2008.

809 You, Y., Huang, C., Gu, J., Li, H., Hao, X., Hou, J.: Assessing snow simulation performance of typical
810   combination schemes within Noah-MP in northern Xinjiang, China. J. Hydrol. 581, 124380,
811   2020.

812

813 **Table 1**. Description of the land surface model, the data used, and assimilation experiment

814   designs.

	INFORMATION	REFERENCES
Land Surface Model	JULES	Best et al., (2011)
Atmospheric Forcing	3-hourly JRA-55 reanalysis	Kobayashi et al., (2015)
Snow Observation	AMSR2 & IMS	Imaoka et al., (2010)
		Ramsay (1998)
		Helfrich et al., (2007)
Data Assimilation scheme	Local Ensemble Transform Kalman Filter (LETKF)	Hunt et al., (2007)
		Miyoshi and Yamane, (2007)
Resolution (km)	0.5° ×0.5° (~ 50)	
	1-day DA cycle	
Localization patch size (km)	3×3 (150), σ =30	
Ensemble sizes	24	
Experiment period	2013-2020, APR	

815

816
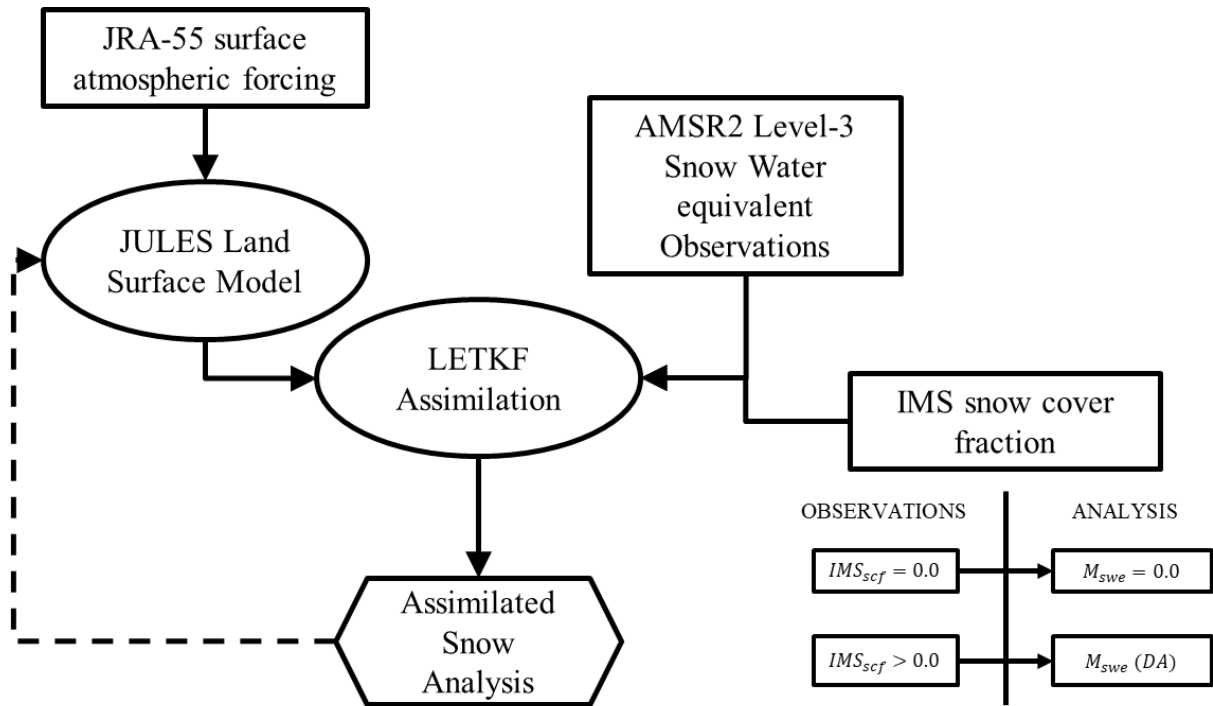
817

818   **Figure 1**. Schematic diagram of the snow assimilation system with satellite-derived

819   observations and the land surface model outputs.

820

821
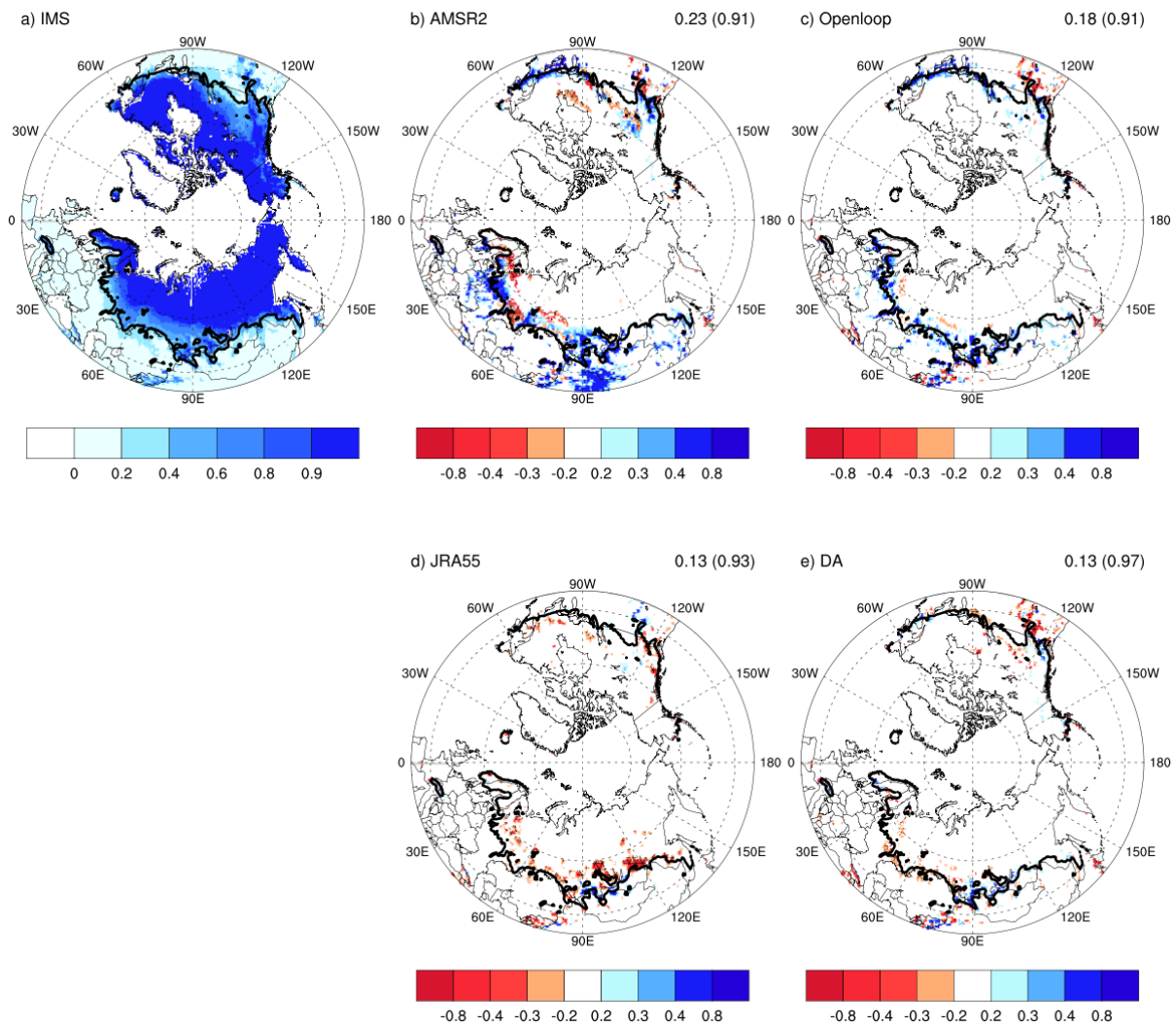
Figure 2. (a) Climatology of SCF from IMS used as reference and (b-e) the differences from IMS for AMSR2, base-line model simulation (Openloop), JRA55, and the data assimilation results (DA) for April during 2013-2020. The black line represents the boundary of the transition region, defined as the climatological-mean SWE of less than 16mm. Each value on the top right is the root-mean-squared difference with IMS and the accuracy from IMS (parenthesis) for 15323 pixels over 40-60°N. The accuracy is defined in supplementary Table 1 as in previous study (Lee et al., 2015). Negative values (areas) in red shades are indicated with hatching. Here, SCF is dimensionless since it represents a proportion rather than a physical measurement with units.

834
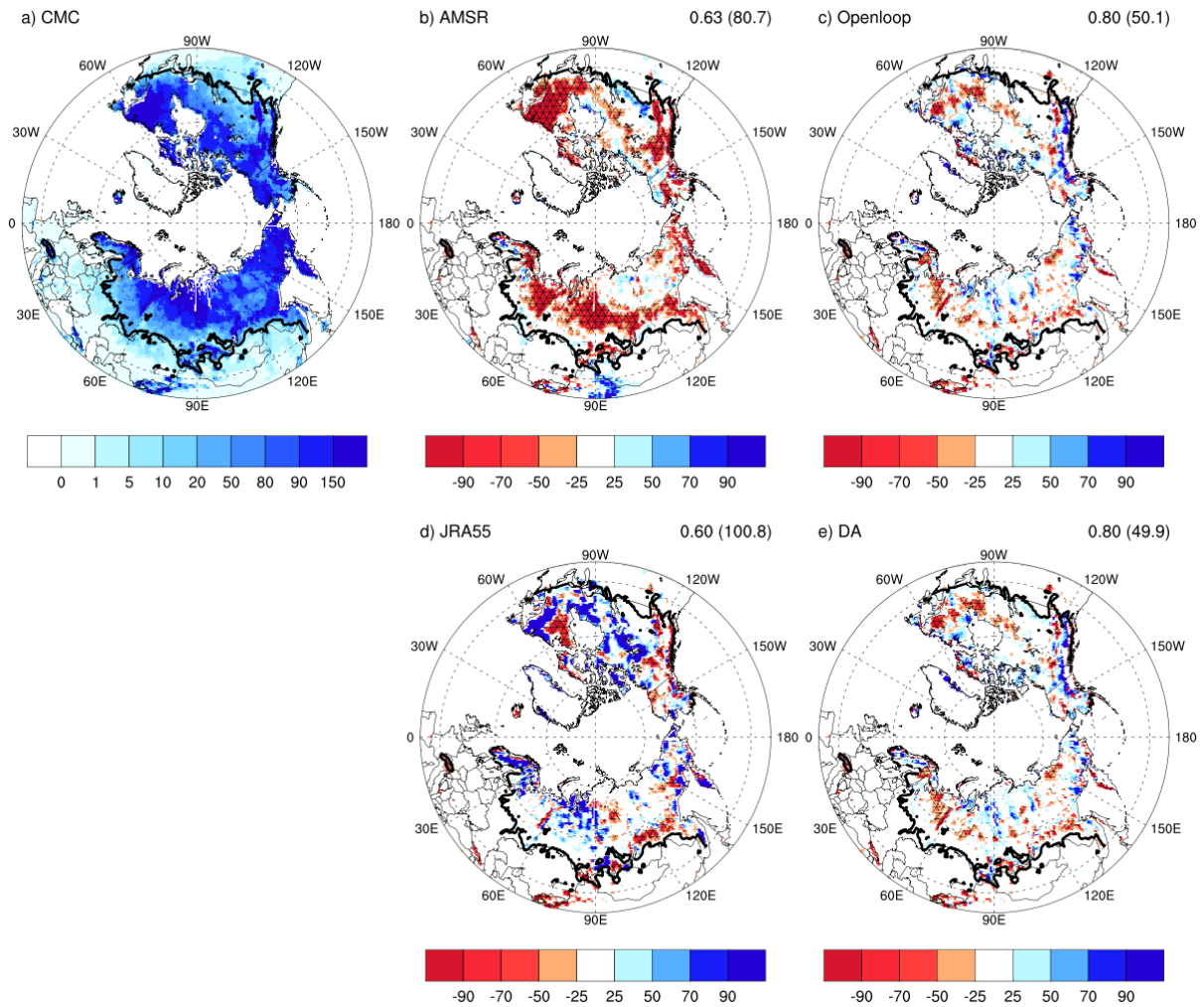
Figure 3. (a) Climatology of SWE (unit: kg/m^2 or mm), from CMC used as reference and (b-e) the differences from CMC for AMSR2, base-line model simulation (Openloop), JRA55, and the data assimilation results (DA) for April during 2013-2020. The black line represents the boundary of the transition region, defined as the climatological-mean SWE of less than 16mm. Each value on the top right is the pattern correlation with CMC for 26482 pixels over 40 $^{\circ}$N and the root-mean-squared difference (unit: kg/m^2 or mm) from CMC (parenthesis) for 15323 pixels over 40-60°N. Negative values (areas) in red shades are indicated with hatching.

843
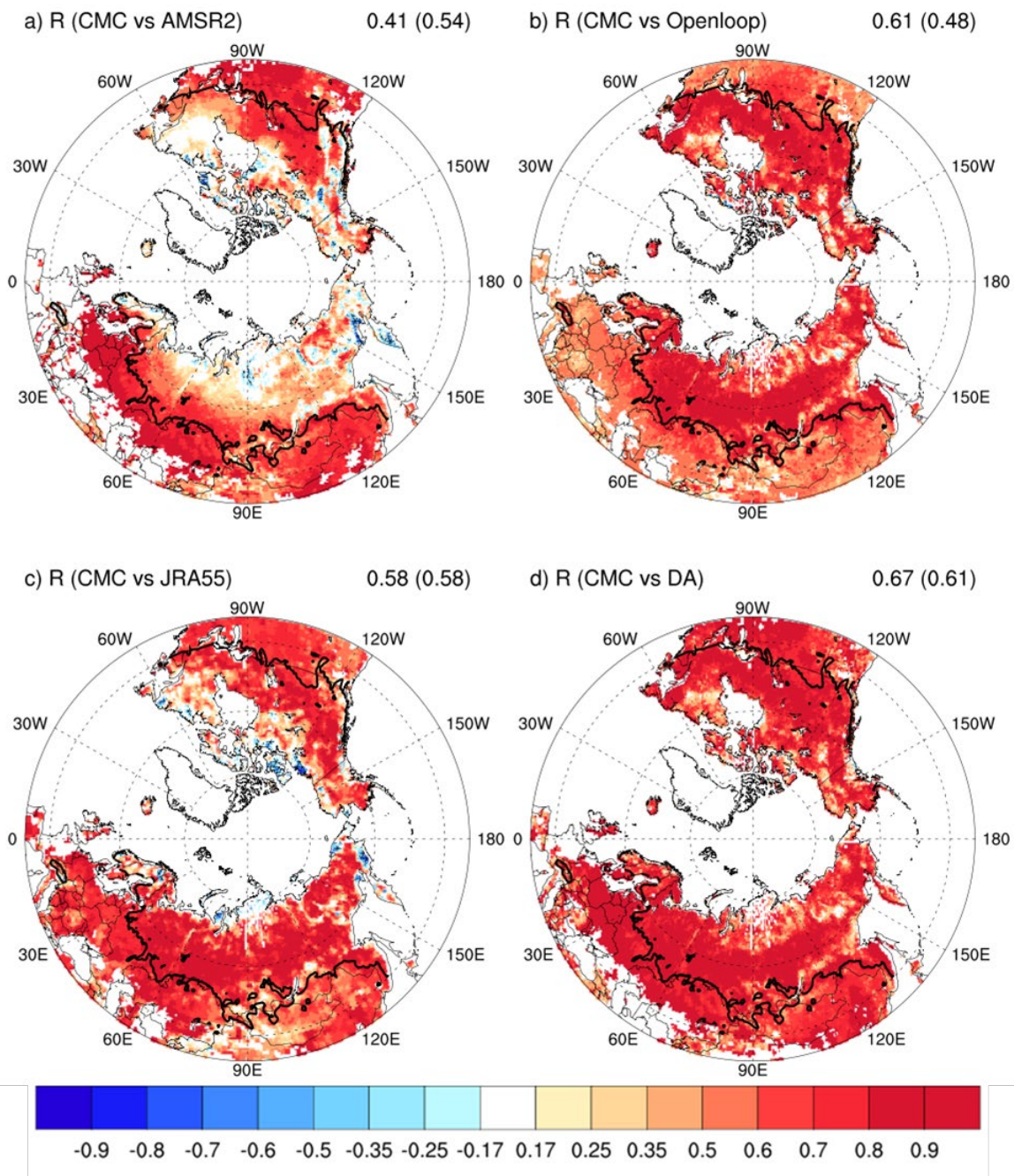
Figure 4. SWE skill measured as the Spearman rank correlation (R) with the CMC for AMSR2, base-line model simulation (Openloop), JRA55, and the data assimilation result (DA). The black line represents the boundary of the transition region, defined as the climatological-mean SWE of less than 16mm. Each value on the top is the area-average R of North hemisphere for 26482 pixels over 40°N and for 8801 pixels over the transition region (parenthesis). Negative values (areas) in red shades are indicated with hatching.
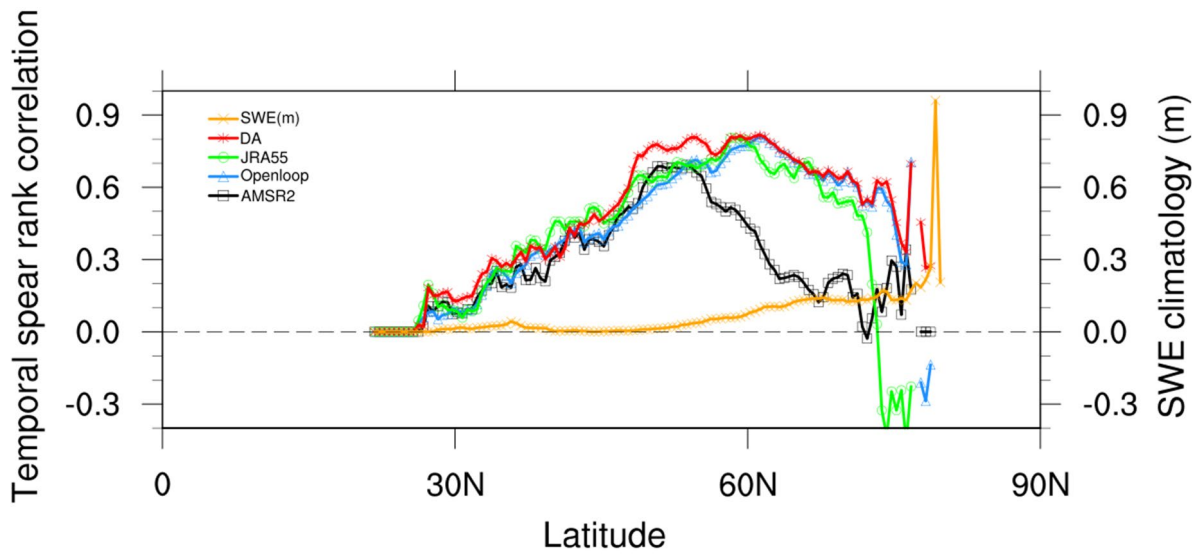
Figure 5. Zonally-averaged Spearman rank correlation (R) along the latitude for SWE. The yellow line indicates the climatology of SWE, and the black, blue, green, and red lines denote the values of AMSR2, base-line model simulation (Openloop), JRA55, data assimilation results (DA), respectively.

858
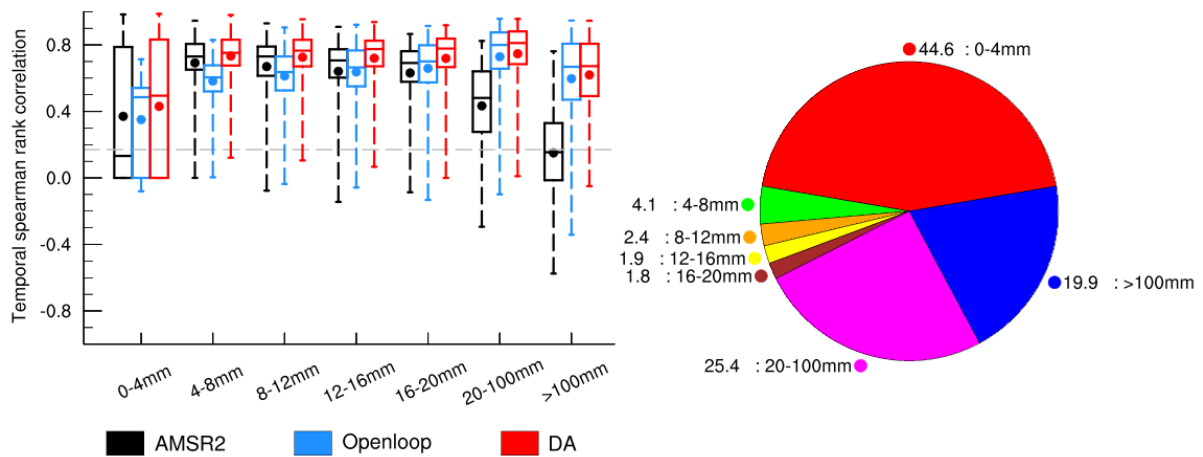
Figure 6. Box plots of the Spearman rank correlation (R) according to SWE (unit: kg/m² or mm). The pie chart shows the total area ratio (%) as a function of SWE amount. The black, blue, and red boxes denote the AMSR2, base-line model simulation (Openloop), and the data assimilation results (DA), respectively. The boxes indicate 25 and 75% percentiles, and the line and point in the boxes shows the median and the mean values. The upper and lower whiskers denote the 10 and 90% percentiles, respectively.

865
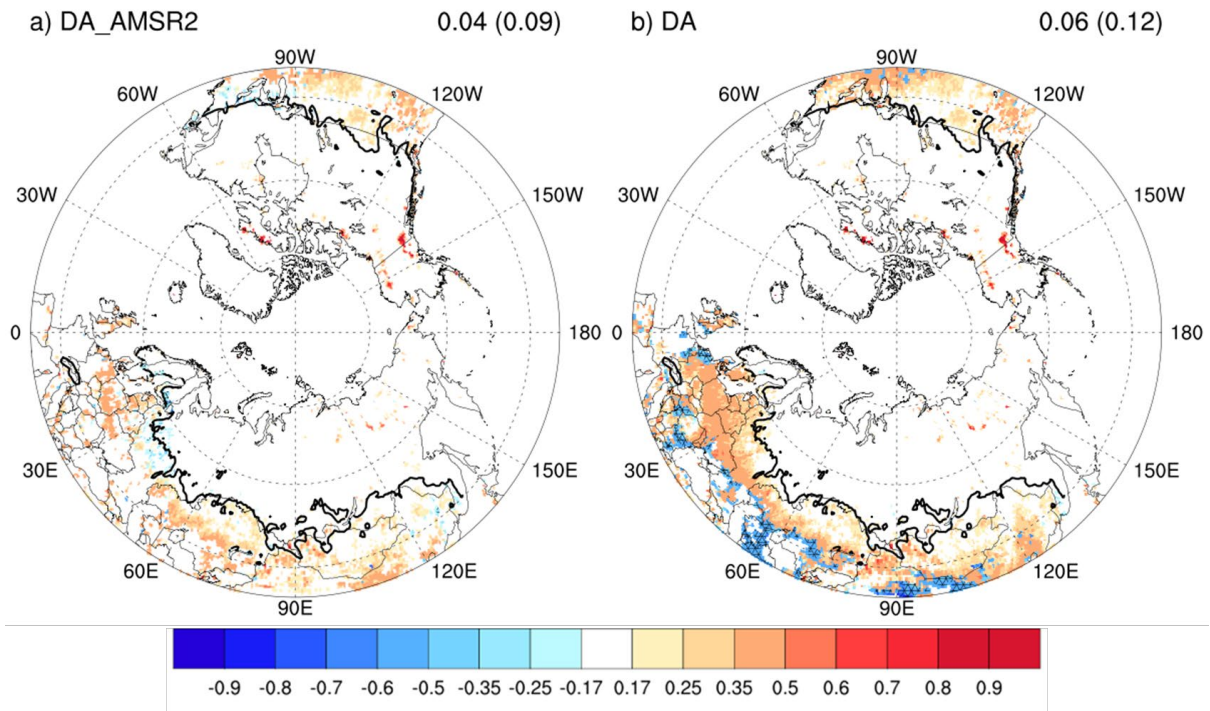
Figure 7. The difference in SWE Spearman rank correlation coefficient with CMC between the Openloop and data assimilation results: DA employing both AMSR2 and IMS and DA_AMSR2 utilizing solely AMSR2 and excluding IMS, for April during 2013-2020. The black line represents the boundary of the transition region, defined as the climatological-mean SWE of less than 16mm. Each value on the top right is the area-average over 40°N and the transition region (parenthesis). Negative values (areas) in red shades are indicated with hatching.
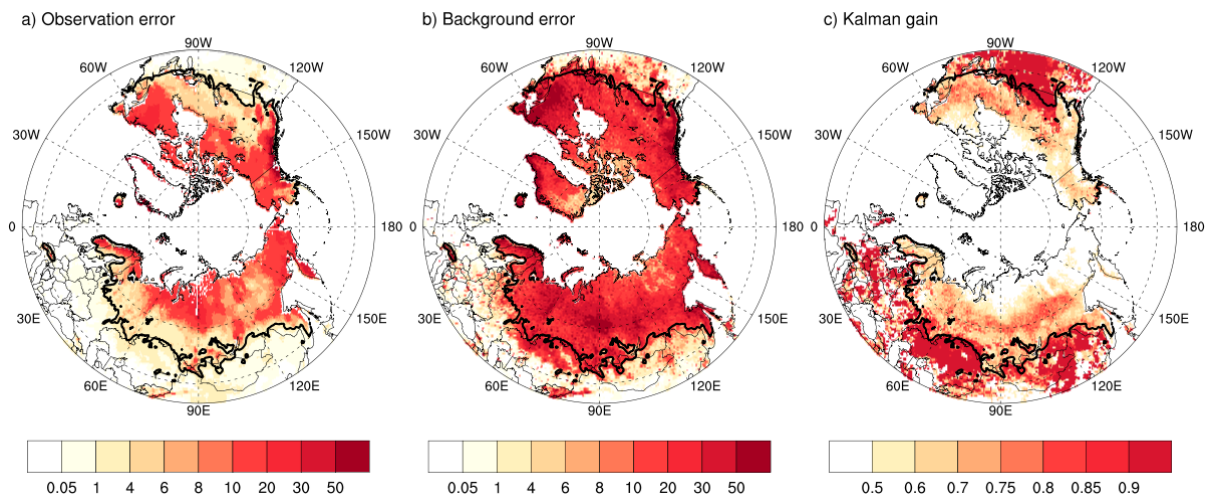
876

877 **Figure 8**. Spatial distribution of observation error (unit: kg/m^2 or mm), background error (unit:

878 kg/m^2 or mm), and Kalman gain. The black line represents the boundary of the

879 transition region, defined as the climatological-mean SWE of less than 16mm.

880

881
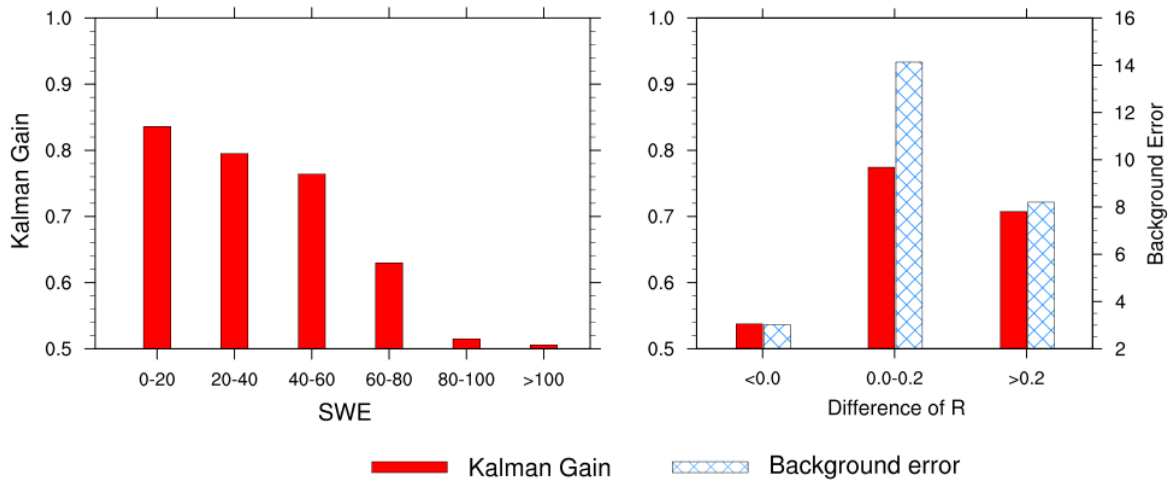
Figure 9. Bar chart of (left) the Kalman gain according to the SWE amount (unit: kg/m^2 or mm)

and (right) the Kalman gain (red line) and background error (blue hatched line) as a

function of the difference between Openloop and DA in Spearman rank correlation

coefficient (R).

886

887
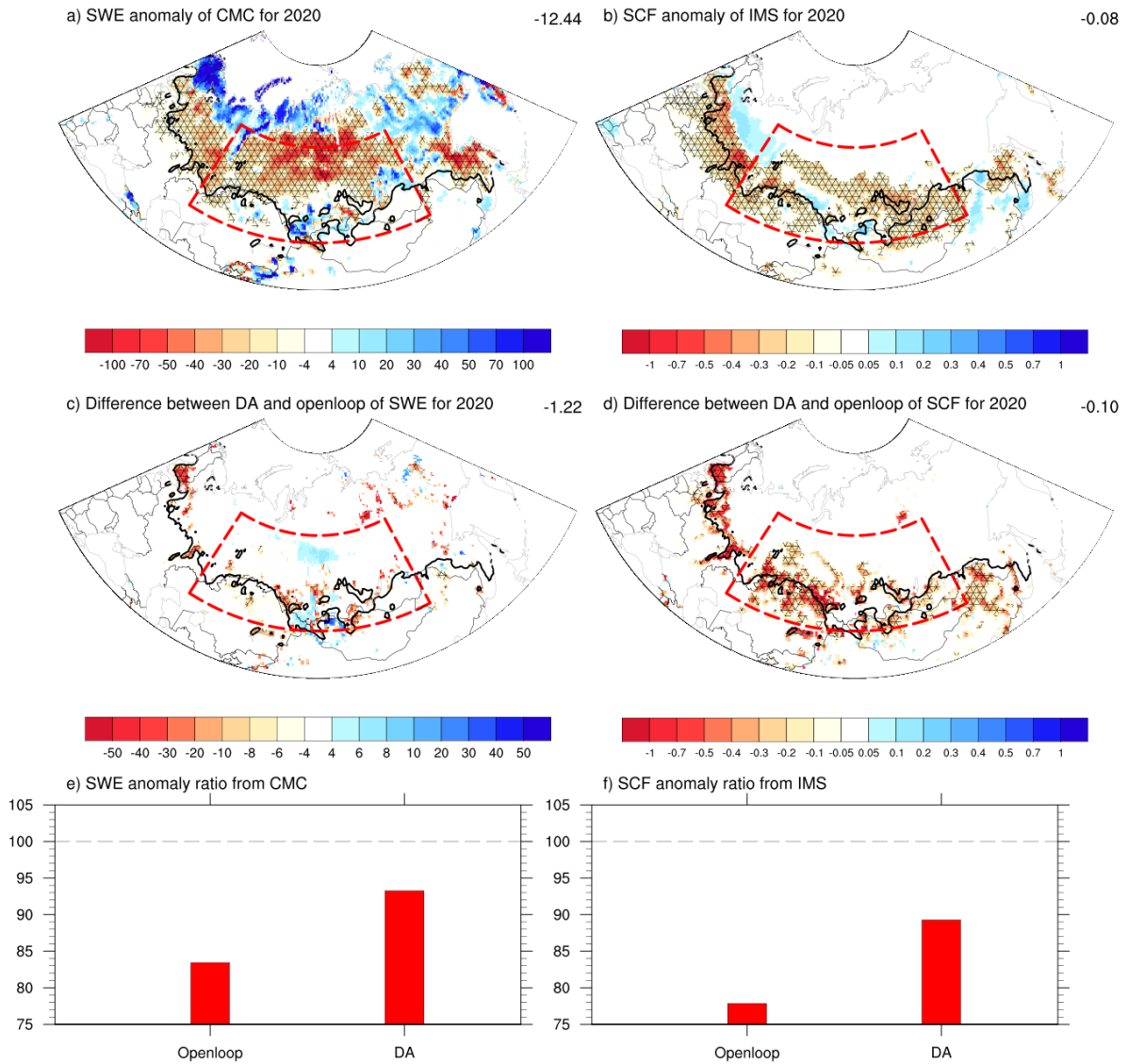
Figure 10. Anomalies of a) SWE (unit: kg/m^2 or mm) from CMC and b) SCF from IMS as well as the difference (c, d) of variables between DA and Openloop in April 2020. Bar chart (e, f) indicates the ratio of DA and Openloop to verification data such as CMC and IMS in the red box (48–65°N and 55–120°E), which is the region associated with extreme high-temperature events, focused on this study. Negative values (areas) in red shades are indicated with hatching.

894